RESEARCH ARTICLE | APRIL 15 2025

Spectral analysis of a low-pressure turbine cascade subject to incoming wakes at high freestream turbulence levels

Jinah Jeun ; Davide Lengani ; Jan Pralits ; Daniele Simoni ; Ardeshir Hanifi ; Dan S. Henningson

Physics of Fluids 37, 044114 (2025)
https://doi.org/10.1063/5.0264219

Physics of Fluids ARTICLE pubs.aip.org/aip/pof

Spectral analysis of a low-pressure turbine cascade subject to incoming wakes at high freestream turbulence levels

Cite as: Phys. Fluids **37**, 044114 (2025); doi: 10.1063/5.0264219
Submitted: 9 February 2025 · Accepted: 31 March 2025 ·
Published Online: 15 April 2025

View Online Export Citation CrossMark

Jinah Jeun,[1,a)] Davide Lengani,[2] Jan Pralits,[3] Daniele Simoni,[2] Ardeshir Hanifi,[1] and Dan S. Henningson[1]

AFFILIATIONS

[1]FLOW, Department of Engineering Mechanics, KTH Royal Institute of Technology, Stockholm, Sweden
[2]DIME, University of Genova, Genova, Italy
[3]DICCA, University of Genova, Genova, Italy

[a)]Author to whom correspondence should be addressed: jeun@mech.kth.se

ABSTRACT

This study employs spectral proper orthogonal decomposition (SPOD) on direct numerical simulation data from a low-pressure turbine (LPT) operating under high freestream turbulence levels. The impacts of upstream wakes on the transition process are assessed by considering both cases with and without wakes, modeled by a moving cylinder placed upstream of the LPT blade. In the absence of upstream wakes, the SPOD eigenvalues decreases almost monotonically as frequency increases. At high frequencies, the spectra reveal a broadband interval with minimal elevation, corresponding to the Kármán vortex streets formed downstream of the blade's trailing edge. The SPOD modes in this inflow condition show fully attached boundary layers across the entire blade, suggesting that the boundary layers may be transitional. When subjected to upstream wakes, however, the SPOD spectra display several intense peaks linked to the wake passage frequencies. The associated SPOD modes reveal turbulent spots and lambda vortices on the rear suction side of the blade, typical indicators of turbulent boundary layers. Between the fundamental passage frequency and its harmonics, a series of tones emerge, representing the Doppler-shifted wakes. Triadic interactions between modes involving upstream wakes and their translation induce a cascade of these intermediate components, as verified by the bispectrum map. The SPOD modes capture interactions of structures carried by upstream wakes and the freestream flow with the blade boundary layers, manifested as low- and high-velocity streaks whose breakdown promotes the transition. High-frequency modes describe coherent structures break down into the vortex streets at the trailing edge.

I. INTRODUCTION

Laminar-to-turbulent transition in fluid flows is a fundamental phenomenon with broad implications in engineering applications. In low-pressure turbines (LPT) of aeroengines, it is of particular importance because it directly affects lift and drag, impacting overall turbine performance.[1] Despite its significance, understanding the transition process and accurately predicting its onset in real turbines remain challenging, as the flow field around a turbine cascade forms a highly complex, three-dimensional, unsteady system governed by numerous interdependent factors. Transition is heavily influenced by deterministic periodic wakes shed from upstream blades, freestream turbulence (FST) intensities, a wide range of scales from high Reynolds numbers *Re*, operating Mach numbers *Ma*, pressure gradients, blade curvature and edge bluntness, as well as flow separation, as summarized in the review papers by Hodson and Howell[1] and, more recently, by Sandberg and Michelassi.[2] Many existing studies have thus focused on isolating individual parameters to identify and quantify their specific impacts on transition, with the aim of simplifying analysis.

Different FST intensities can lead to completely distinct transition scenarios. On the rear suction side of a high-lift LPT blade, strong adverse pressure gradients can cause the formation of a separation bubble or lead to boundary layer separation. Under low FST intensities, shear layers typically fail to reattach before reaching the trailing edge. Detached shear layers then roll up and evolve into large-scale vortices via the Kelvin–Helmholtz instability, with fragmentation of these coherent structures initiating transition within the separated shear layers.[1,3–8]

Under high FST intensities, flow separation is typically suppressed, or, in the case of separation, reattachment of previously separated shear layers may even occur. Upstream turbulence in the low-frequency range penetrates the blade boundary layer via shear sheltering mechanisms as discussed by Jacobs and Durbin,[9] resulting in the formation of low- and high-velocity streaks beyond the velocity peak of the blade's suction side, also known as Klebanoff modes.[10–12] These streaky structures have been studied extensively in simple geometries.[13–18] Through lift-up mechanisms, the elongated, streamwise-oriented structures develop into turbulent spots near the rear part of the blade, driven by sinuous and/or varicose instabilities, and ultimately transition into fully turbulent flow.[8,19–24] This scenario represents a bypass transition, where the flow bypasses pre-transitional stages typical of the classical transition process involving the Tollmien–Schlichting waves.

Geometric illustrations of periodic incoming wakes are thoroughly discussed using both experimental and numerical data.[5,25–28] These studies describe how wakes bow and stretch in the inter-blade region due to curvature and velocity fluctuations, migrate toward the boundary layers as they convect downstream, and ultimately flush away past the trailing edge. Periodic wakes introduce low-frequency components tied to their passage, yet also contribute to high-frequency stochastic turbulence. Additionally, upstream wakes may generate alternating elongated streaks along the pressure side of the blade, interacting with Klebanoff modes induced by FST penetrating into the blade boundary layers.[29]

With advances in computing power, large-eddy simulations (LES) have become practical for designing high-lift LPT blades. Researchers have even been able to conduct multi-stage turbine simulations, albeit with simplified geometries.[30] LES offers high-fidelity computations at a reasonable cost by resolving a broader range of scales than Reynolds-averaged Navier–Stokes methods, which assumes unsteadiness on the mean field, often leading to inaccurate predictions in turbomachinery applications.[31] However, LES still leaves sub-grid scales unresolved, which are essential for accurately assessing the turbulent kinetic energy (TKE) budget (particularly in terms of dissipation and transfer rates between scales in the rear part of the blade). Direct numerical simulations (DNS), although more computationally demanding, can capture these small-scale dynamics, providing deeper insights into the complex behavior of turbulent flow in such systems.

Proper orthogonal decomposition (POD)[32] has proven to be an effective tool for analyzing the flow dynamics of LPTs by reducing the high degrees of freedom characterizing flow data. POD generates a series of orthogonal modes by solving an energy-maximization problem under a chosen norm, ranking modes by their energy content. Low-order modes reveal the dominant coherent flow structures that capture the essential flow physics of a system, and a clear separation between low- and high-order modes suggests low-rank behavior in the flow. For example, Lengani and Simoni[8] used POD to investigate dominant coherent structures linked to transition within the blade boundary layer at different FST intensities. The effects of upstream wakes and their interaction with the blade boundary layer were also effectively characterized using POD.[27,29] Lengani *et al.*[29] found that upstream wakes enhance the growth of streamwise-oriented streaks at high FST intensities. In later work, the same authors also analyzed the impacts of reduced frequency on transition.[33]

It is well-established that POD is an effective method for understanding the flow dynamics of a LPT cascade. However, mode shapes resulting from POD are optimal solely in space, averaging over frequency-domain information. An LPT system with significant spectral features—such as low-frequency periodic upstream wakes and structures generated by FST penetrating within blade boundary layers via shear sheltering—could benefit from the recent development of spectral POD (SPOD). SPOD, as the name suggests, extends the classical space-only POD by allowing for spatiotemporal localization of flow structures. While POD has been widely applied to studying flow evolution in LPT cascades, SPOD has been less explored in this context. One notable example is the work of Fiore *et al.*,[34] who applied SPOD to LES data of an LPT subject to upstream wakes at two different *Re*. In this study, LES solved full compressible Navier–Stokes equations, but the authors employed a component-wise SPOD approach. Additionally, Biassoni *et al.*[35] focused on the implementation of a high-performance SPOD algorithm, enabling more efficient analysis of the transport equations in high-fidelity turbomachinery simulations.

This work aims to study flow dynamics of a LPT cascade operating under elevated FST levels by applying SPOD onto existing DNS databases. To explore the effect of upstream wakes, both databases with[36] or without[37] wakes are utilized. Upstream wakes are commonly modeled using a moving cylinder in many experimental and computational work. While previous DNS implementations typically include upstream wakes by specifying time-dependent inflow conditions at the boundary,[3,25,26,38,39] De Vincentiis *et al.*[36] incorporated an upstream cylinder directly into the simulations through communications of two overlapping grids corresponding to the cylinder and the blade.

The remainder of the present paper is organized as follows. Section II presents the flow configuration of the LPT cascade under consideration. Section III introduces the DNS database and outlines its post-processing through SPOD. The mean and instantaneous flow fields are visualized in Sec. IV, followed by the SPOD for the steady inflow condition (in the absence of upstream wakes) in Sec. V. In Sec. VI, the results of SPOD for the unsteady inflow condition with upstream wakes are presented. Finally, Sec. VII concludes the paper with a summary and some remarks.

II. FLOW CONFIGURATION

Figure 1 shows a schematic representation of the LPT blade studied in the present work. Following the experimental work of Lengani *et al.*,[29] we examine the same LPT blade subject to periodically incoming wakes, which are modeled by a moving cylinder. Throughout this paper, the system is normalized by the axial chord length $c_x = 0.095$ m and the inlet velocity $u_{in} = 5.92$ m/s, serving as the reference length scale and the reference velocity scale, respectively. The trailing edge thickness of the blade $t = 0.02c$ is relatively sharp. The inlet angle of attack α is measured as 40° relative to the axial axis. The moving cylinder with a diameter $D = 0.0316c_x$ is placed at a distance $d_c = 0.347c_x$ upstream of the LPT blade's leading edge. The blade pitch g is set as $0.685c_x$, which also defines the spacing between consecutive cylinders, resulting in the cylinder passage period of $T_{cp} = 0.756$. To save computational resources, the cylinders are located closer together in the numerical simulations than in the experimental setup, where it was one and a half times the blade pitch. The translation velocity of the cylinder is given as $u_c = (0, -1.145, 0)$. The Reynolds number is

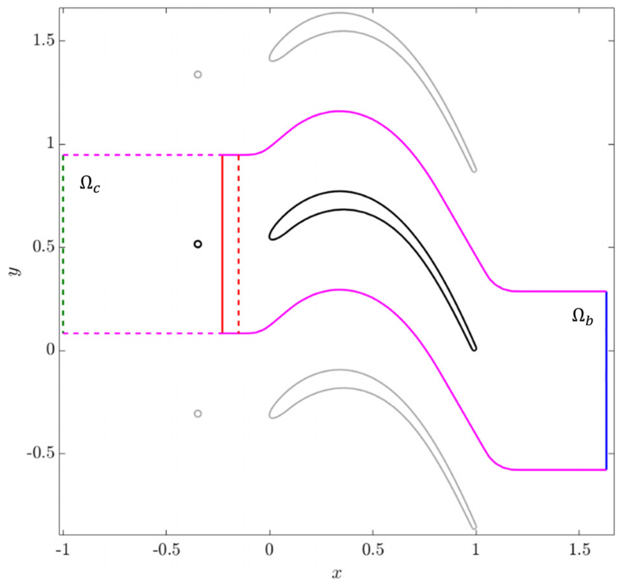

FIG. 1. A schematic representation of the LPT blade subject to the upstream wakes modelled by a row of moving cylinders. Dashed lines indicate the computational domain for the cylinder Ω_c, while solid lines represent that for the turbine blade Ω_b. Reproduced from De Vincentiis *et al.*, J. Turbomach. 145, 051011 (2023); licensed under a Creative Commons Attribution (CC BY) License.

computed using the axial cord length and the inlet velocity as $Re = u_{in}c_x/\nu = 40\,000$, where ν is the kinematic viscosity of the air at 20 °C. This value is equivalent to the experimental Reynolds number of 70 000, which was based on the chord length c and the isentropic velocity at the cascade outlet and chosen to represent small to medium sized aeroengines under cruise conditions.

To investigate the effects of the upstream wakes, we also consider a steady inflow condition described by a stand-alone LPT blade with identical geometric characteristics. DNS data for this case were obtained from Đurović *et al.*[37] and compared with the companion experiment conducted by Lengani and Simoni.[8]

In both inflow cases, the FST levels were high with the turbulence intensity of $Tu = 5.2\%$.

III. METHODOLOGY

A. Direct numerical simulations

In this work we utilize the DNS data of the LPT cascade under high FST levels for spectral analysis. The evolution of the fluid flow around the LPT cascade was simulated by solving the incompressible Navier–Stokes equations, given that the local Mach number in the domain remains less than 0.1

$$\frac{\partial \mathbf{u}}{\partial t} + \mathbf{u}\cdot\nabla\mathbf{u} = -\nabla\mathbf{p} + \frac{\mathbf{1}}{\mathbf{Re}}\nabla^2\mathbf{u}, \tag{1}$$

$$\nabla\cdot\mathbf{u} = \mathbf{0}. \tag{2}$$

The DNS was performed using the open-source code `Nek5000`.[40] This code solves the weak form of the governing equations using the spectral element method, which provides geometric flexibility while achieving the high accuracy characteristic of spectral methods. The numerical domain was discretized using hexahedral elements, following the $\mathbb{P}_N - \mathbb{P}_{N-2}$ formulation.[41] In each element, the velocity is represented using high-order Lagrange interpolants on the $N_p + 1$ Gauss–Lobatto–Legendre quadrature points, while the pressure is discretized on the $N_p - 1$ Gauss–Legendre quadrature points. For the DNS data used in this study, a polynomial order of $N_p = 9$ was adopted. The equations were advanced in time using a third-order extrapolation scheme (EXT3) for the nonlinear terms and a third-order backward differentiation scheme (BDF3) for the viscous terms.

To include the upstream wakes, the `Nek-Nek` framework within the `Nek5000` was modified in order to be able to perform simulations in two different frames of reference interacting with each other. One simulation was conducted in the reference frame of the moving cylinder (Ω_c), represented by the dashed line in Fig. 1, and the other in the reference frame of the stationary LPT blade (Ω_b), denoted by the solid line in the same figure. The two simulations communicated at the outlet of the cylinder domain and the inlet of the blade domain to account for the translation of the cylinder.

At the inlet of the cylinder domain, a Dirichlet boundary condition was applied. Along with the inlet velocity $u_{in} = (\cos\alpha, \sin\alpha, 0)$, divergence-free FST was imposed as a superposition of Fourier modes with random phase shifts using a method similar to that proposed by Schlatter[42]

$$\boldsymbol{u_T} = \sum_{k_x,k_y,k_z} A(k)\hat{\boldsymbol{u}}_n(k_x,k_y,k_z)e^{\mathrm{i}(k_x x + k_y y + k_z z - \omega t)}, \tag{3}$$

where (k_x, k_y, k_z) are the three components of the wavenumber vector $\boldsymbol{k}$, $A(k)$ is the scaled amplitude of the freestream mode, k is the magnitude of the wavenumber vector, $\hat{\boldsymbol{u}}_n$ is the normalized Fourier amplitude, and $\mathrm{i} = \sqrt{-1}$ is the imaginary unit. In addition, the angular frequency of disturbance ω can be modeled based on Taylor's frozen turbulence hypothesis. To achieve homogeneous isotropic turbulence, the wavenumber space was divided into 80 concentric spherical shells, and 40 points were randomly selected on each shell. Points on the same shell share the same wavenumber amplitude, with the location of each point representing the three components of a different wavenumber vector. The amplitude of the freestream modes on each shell was then scaled to match the von Kármán spectrum

$$E(k) = Tu^2 u_{in}^2 \Lambda_I \frac{1.606(k\Lambda_I)^4}{\left[1.350 + (k\Lambda_I)^2\right]^{17/6}}, \tag{4}$$

where E is the kinetic energy, Λ_I is the nominal integral length scale, and k is the magnitude of the wavenumber vector. Once the nominal integral length scale and the targeted turbulence intensity were prescribed, the energy was equally distributed over the selected 40 modes on each shell.[18] In our DNS, the turbulence intensity Tu of 5.2% was chosen to reproduce the high FST case in the companion experiment with the nominal integral length scale set to $\Lambda_I = 0.105c_x$. A no-slip boundary condition was applied on the solid boundaries of the cylinder and on the LPT blade. Periodic boundary conditions were imposed along the lateral boundaries (highlighted by the magenta lines in Fig. 1) and in the spanwise direction. Finally, a stress-free boundary condition was used at the outlet of the blade domain.

For both domains, the spanwise width was $L_z = g/2$, and the lateral extent corresponded to one blade pitch g. In the streamwise direction, the numerical domain extended from $x = -1.05$ to 1.6, with the leading edge positioned exactly at $x = 0$. The cylinder domain comprises 113 610 spectral elements, while the turbine domain is meshed using 134 340 elements. The mesh design can be characterized in terms of viscous units, where the viscous length is given by $l^* = \nu/u_\tau$ and the friction velocity is $u_\tau = \sqrt{\tau_w/\rho}$ with τ_w being the wall shear stress and ρ being the fluid density. Scaled by the viscous units, the grid spacing around the turbine blade was $\Delta\xi^+ < 17$ in the streamwise direction and $\Delta\eta^+ < 0.4$ in the wall-normal direction. In the cylinder domain, the streamwise spacing was $\Delta\xi^+ < 6.0$, and the wall-normal spacing was $\Delta\eta^+ < 0.6$. For both domains, the spanwise spacing was maintained at $\Delta z^+ < 7$.

The steady simulations were conducted similarly in the absence of a moving cylinder. The domain extended from $x/c = -0.5$ to 1.3 in the streamwise direction, with the spanwise width of $L_z/c = g$. Only the flow past one blade was computed in the lateral direction, utilizing periodic conditions. At the domain inlet, the same FST generation technique was applied. The generated FST followed a power-law decay downstream, with a decay rate comparable to that of isotropic grid turbulence. The variance of the averaged fluctuation intensities across the three velocity components remained below 5% over the streamwise extent upstream of the LPT blade A similar meshing strategy to that used in the unsteady simulation was implemented to ensure that the criteria for properly resolving the turbulent flow were met, as suggested by Schlatter *et al.*[43] The streamwise spacing ranged from $\Delta\xi^+ = 0.3$ to 4.2, while the wall-normal spacing on the blade surface was $\Delta\eta^+ = 0.7$, increasing progressively toward the boundaries. The spanwise spacing was uniform as $\Delta z^+ = 6$, resulting in the final mesh consisting of 310 366 elements. For a direct comparison between the two simulations with different inflow conditions and to analyze the effects of the upstream wakes, sampled snapshots of the steady inflow case were interpolated onto the unsteady mesh using the *gfldr* subroutine already implemented in `Nek5000`.

More details about the unsteady simulations, including the treatment of the overlapping grids, can be found in De Vincentiis *et al.*[36] Readers interested in the steady simulations and a comprehensive introduction to the FST generation are directed to Đurović *et al.*[37]

B. Spectral proper orthogonal decomposition (SPOD)

SPOD[44] extends the classic proper orthogonal decomposition to extract orthogonal modes in the sense of a spatiotemporal inner product. At a given frequency, SPOD modes are ranked according to their energy contribution within the volume of interest, which depends on the choice of norm defined via a weight matrix. Since the flow dynamics of the LPT cascade are governed by the incompressible Navier–Stokes equations, an integral energy (TKE) norm is employed in this work. The contribution of the spanwise velocity component w is minimal compared to that of the axial u and transverse v components.[34] To reduce computational resources required, only the fluctuations of the axial and transverse velocities are incorporated in the state vector used for SPOD.

At a given frequency f_k, SPOD addresses an eigen-decomposition problem defined by

$$Q_{f_k}^H W Q_{f_k} \Theta_{f_k} = \Theta_{f_k} \Lambda_{f_k}, \tag{5}$$

where Q_{f_k} is the data matrix containing the spatial distributions of the Fourier coefficients at f_k obtained through the temporal Fourier transform of several segments of the flow snapshots, and W represents the weight matrix, which accounts for the choice of inner product and the quadrature weights. In addition, the superscript H indicates the complex conjugate transpose.

In practice, the flow snapshots are divided into several overlapping segments using Welch's method.[45] The eigen-decomposition of the cross-spectral density matrix $C = Q_{f_k}^H W Q_{f_k}$ results in the matrix Θ_{f_k}, which consists of the resulting eigenvectors as its columns, and the diagonal matrix Λ_{f_k}, which stores the modal energy. The SPOD modes Φ_{f_k} are then computed as follows:

$$\Phi_{f_k} = Q_{f_k} \Theta_{f_k} \Lambda_{f_k}^{-1/2}. \tag{6}$$

It is worth noting that we solve a variant of the standard SPOD by utilizing the method of snapshots.[46] Given that the number of realizations N_t is significantly smaller than the degree of freedom in space N_x, the eigen-decomposition can be performed more efficiently in this way.

The data matrix Q is pre-saved in the storage before performing the eigen-decomposition to manage computational resources efficiently. For the unsteady inflow case with the periodic wakes from the upstream cylinder, $N_t = 1291$ flow snapshots are divided into seven segments, each containing $N_{fft} = 480$ snapshots with 75% overlap. In this way, each data segment corresponds to six cylinder passages, which is sufficient to capture physics underpinning the LPT cascade system. After applying the discrete Fourier transform, the resulting frequency resolution of the flow segment is reduced to $\Delta St = 0.22$, where the Strouhal number St is defined based on the inlet velocity u_{in} and the axial cord length c_x as $St = fc_x/u_{in}$. To match this resolution, the flow segment for the steady inflow case consists of $N_{fft} = 430$ snapshots. With the same 75% overlap between segments, a total of 981 flow snapshots result in six SPOD modes at a given frequency. In both cases, each flow segment is windowed using a Hamming function to minimize spectral leakage.

Note that, as described in the above, the actual SPOD is performed in the Cartesian coordinates. To obtain the modes aligned in the streamwise direction, the resulting SPOD modes are rotated by the appropriate time-mean angle to recover the streamwise u_r and the wall-normal v_r components.

IV. MEAN AND INSTANTANEOUS FLOW FIELDS

Figure 2 presents the time-averaged flow field around the LPT blade for both cases: (a) without and (b) with incoming wakes. The normalized streamwise velocity field is derived from the axial and wall-normal velocity components, with contours extracted at the midspan of the LPT blade ($z/x_c = 0$). Magnified views of the blade boundary layers near the trailing edge are provided in the upper-right corner of each sub-figure. The inflow has an angle of approximately $\alpha = 40°$ at the domain inlet follows the blade curvature as it convects downstream. The flows are exposed to the strong adverse pressure gradient behind the velocity peak on the blade suction side. Owing to the high FST experienced in both cases, boundary layer separation is suppressed, unlike in LPT blade flows subjected to low FST intensities. Subject to periodic upstream wakes, the unsteady inflow case shows higher velocity gradients near the wall and thicker boundary layers, attributed to wake-boundary layer interactions (see also Figs. 6 and 10

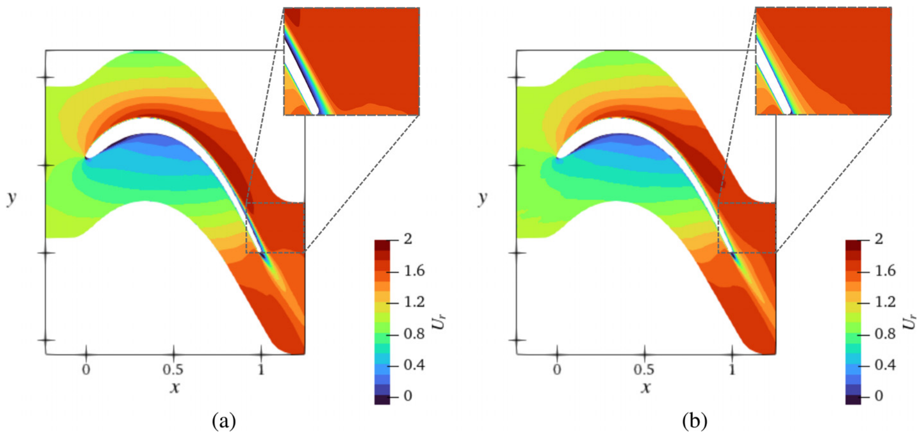

FIG. 2. The time-averaged flow field around the LPT blade for: (a) steady inflow condition without incoming wakes and (b) unsteady inflow condition with incoming wakes. Contours are visualized using the normalized streamwise velocity. Enlarged boxes in the upper right corner of each sub-FIG magnify the boundary layers near the blade trailing edge.

of De Vincentiis *et al.*[36] for the mean and root mean square velocity profiles). This implies an earlier onset of a turbulent boundary layer state along the blade suction side. The velocity peak in this case is located at $x/c_x = 0.683$, slightly downstream compared to the case without incoming wakes.

The instantaneous flow fields at $z/x_c = 0$ for both cases are depicted in Fig. 3. The contours represent streamwise velocity fluctuations, normalized by the inlet velocity. Under steady inflow conditions, the flow field exhibits multi-scale structures randomly distributed throughout the domain. Within the boundary layer, elongated low-speed streamwise structures induced by high-intensity FST are observed. Their breakdown into fine-scale stochastic structures leads to the transition to turbulence before the flow exits the trailing edge. In contrast, Fig. 3(b) describes the flow field around the LPT blade under the influence of incoming wakes. The wakes impinge the blade leading edge and advect downstream toward the blade trailing edge, generating positive and negative velocity perturbation regions around the blade. These alternating velocity perturbation regions are also imprinted on the boundary layer. Along with the migration of periodic wakes, the high FST induces elongated streamwise streaks within the boundary layers. The breakdown of these streaky structures occurs earlier than in the case of steady inflow condition, promoting an anticipated transition to turbulence.[29]

Further details on the mean and instantaneous characteristics of the flows, including pressure coefficients, skin friction coefficients, and root mean square values, can be found in Đurović *et al.*[37] and De Vincentiis *et al.*[36]

V. SPOD FOR THE STEADY INFLOW CONDITION (WITHOUT INCOMING WAKES)

In this section, SPOD is applied to the flow data obtained under the steady inflow condition, with the region near the domain outlet omitted to reduce computational demands. The resulting SPOD energy spectra, shown in Fig. 4, are plotted against the Strounal number defined as $St = fc_x/u_{in}$. The SPOD eigenvalues display a nearly monotonic decrease with increasing frequency, signifying the absence of highly energetic tonal phenomena, as the turbine blade is primarily influenced by isotropic FST. The close proximity of the leading SPOD eigenvalue to the second one further supports the lack of a dominant physical phenomenon in this case.

Figure 5 identifies the leading SPOD modes visualized via isosurfaces colored by the real part of the streamwise velocity component, selected at (a) $St = 1.323$ and (b) $St = 3.308$, respectively. While the computed SPOD mode also includes the wall-normal velocity components as explained in Sec. III B, we have chosen to focus exclusively on the streamwise velocity component throughout this paper for brevity, as both components generally provide similar insights. To recover the inter-blade region, the SPOD modes computed within a single blade pitch domain are replicated under the periodic boundary condition in the lateral direction. Without the influence of cylinder wakes, the flow

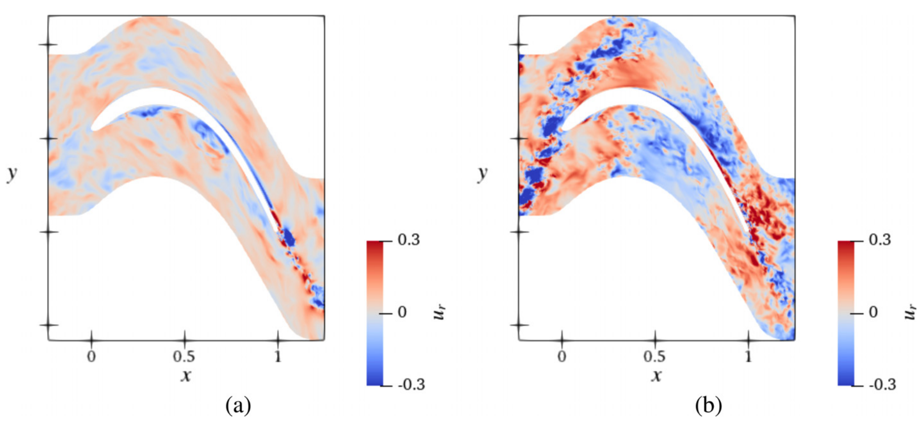

FIG. 3. Instantaneous streamwise velocity perturbations around the LPT blade: (a) steady inflow condition without incoming wakes and (b) unsteady inflow condition with incoming wakes.

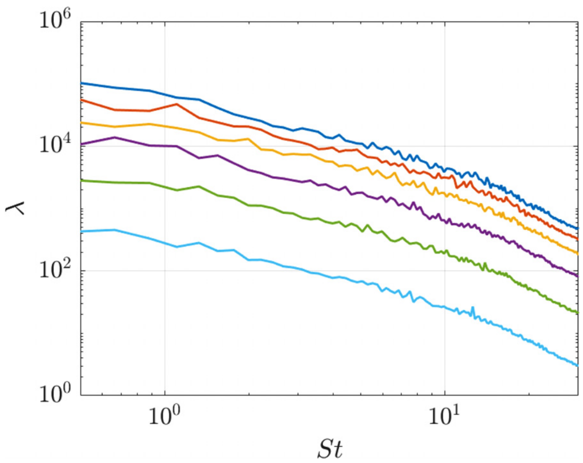

FIG. 4. SPOD energy spectra obtained from flow fluctuations for the steady inflow case, including both axial and transverse velocity fluctuations. No tonal peaks are observed within the relevant frequency range.

structures stretch along the blade curvature as they are convected downstream, leaving the trailing edge without further generating coherent structures. Due to the high intensity FST, a multitude of structures with various scales is distributed around the LPT blade, especially near the blade leading edge.

Figure 6 highlights mode shapes near the blade boundary layers, showcasing elongated low- and high-velocity streamwise streaks generated by the penetration of the elevated freestream turbulence. At $St = 1.323$, spanwise-modulated negative velocity perturbation structures appear downstream of the velocity peak position on the blade suction side, which evolve into streamwise streaks as they convect further downstream. These structures exhibit smaller scales at higher frequency ($St = 3.308$). The blade boundary layers remain attached, potentially transitioning to turbulence through the breakdown of the streaks. Indeed, these modes (appearing in the low- to mid-frequency ranges) characterize the interaction between the freestream turbulence and the boundary layers on both sides of the blade. Figure 7 illustrates large-wavelength streamwise-aligned structures on the rear pressure side of the blade, formed by this interaction.

To better understand the SPOD energy spectra in the absence of any energetic spectral peaks, we opt to repeat SPOD on different sections of the turbine blade domain, splitting the original volume of interest into 20 sub-regions. As shown in Fig. 8, the turbine blade domain is partitioned to allocate a similar number of grid points to each zone for fair computational resource distribution, while preserving specific geometric features within each zone to capture the dominant physical mechanisms unique to different regions of the LPT domain.

Under isotropic FST, the SPOD spectra generally exhibit similar profiles across zones, with the notable exception of zone 20 near the trailing edge. While high-frequency components carry progressively less energy in other sub-zones as seen in the full domain analysis, the energy spectra reveal a broadband range of $St = [5, 15]$ in zone 20 as described in Fig. 9.

Inspired by this, we examine the SPOD mode shapes within this frequency, for instance, at $St = 10.60$. As given in Fig. 10, at this frequency, the von Kármán vortex rolls are observed, while flow structures upstream of the blade leading edge appears to be weak.

VI. SPOD FOR THE UNSTEADY INFLOW CONDITION (WITH THE INCOMING WAKES)

A. In the cylinder domain

To identify spectral characteristics associated with the cylinder wakes, SPOD is employed onto the flow field extracted in the reference frame of the upstream cylinder. Focusing on the wakes induced by the cylinder movement, the domain of interest is restricted to the downstream region of the moving cylinder. Figure 11 visualizes the resulting SPOD energy spectra as a function of the Strounal number St. Several distinct peaks appear in the spectra, corresponding to the translation of the cylinder and the vortices shed behind it. Given the cylinder passage period of $T_{cp} = g/u_c = 0.7557$, a spectral peak is observed at $St = (1/T_{cp})c_x/u_{in} = 1.323$. On the other hand, as

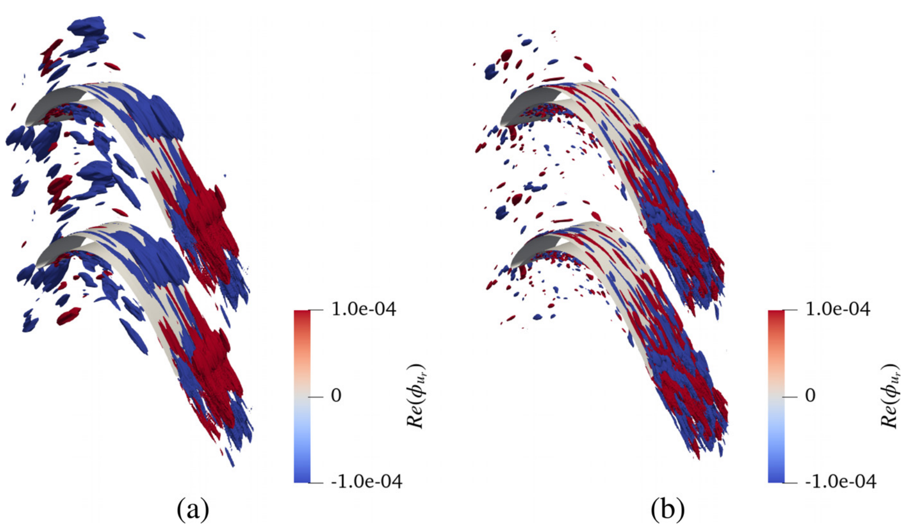

FIG. 5. The leading SPOD modes computed for the steady inflow case. Mode shapes are visualized via isosurfaces colored by the real part of the streamwise velocity components: (a) $St = 1.323$ and (b) $St = 3.308$.

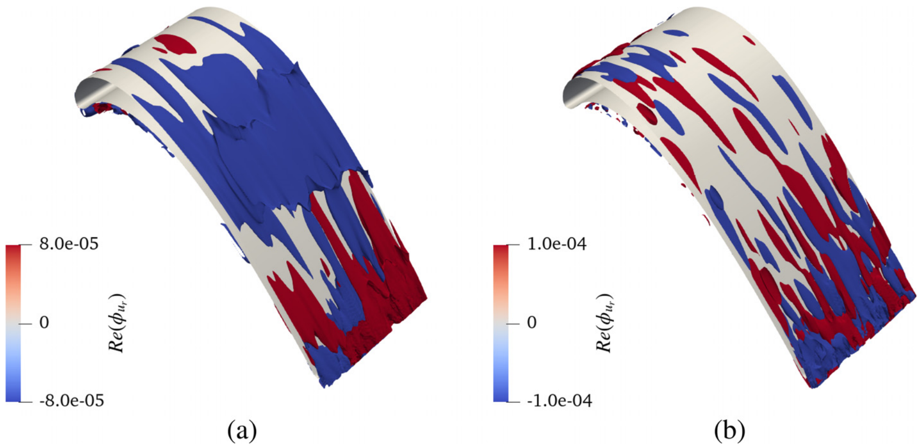

FIG. 6. The leading SPOD modes highlighted in the blade boundary layer region for the steady inflow case. Mode shapes are visualized via isosurfaces colored by the real part of the streamwise velocity components: (a) $St = 1.323$ and (b) $St = 3.308$.

illustrated by the leading mode shape in Fig. 12, the most prominent peak at $St = 12.57$ is linked to the cylinder wakes. Using the Strounal number defined by the cylinder diameter d_c and the relative velocity $u_{rel} = \sqrt{(u_{in}\cos\alpha)^2 + (u_{in}\sin\alpha + u_c)^2}$, this value translates to $St_c = fd_c/u_{rel} = St(d_c/c_x)(u_{in}/u_{rel}) = 0.2041$, closely aligning with the typical vortex shedding frequency for a circular cylinder.[47] The leading mode shape reveals alternating high- and low-velocity vortical structures, elongated vertically relative to the shedding direction, resembling those computed in previous studies.[48,49] This mode carries significantly more energy than both higher-order modes at the same frequency and modes at other frequencies, highlighting the dominant impact of the cylinder wakes. By taking the spatial FFT of the wakes along their propagation direction, the primary wavenumber is identified at $k_{cw} = 45.60$, leading to the phase speed of $u_{p,cw} = \omega/k_{cw} = 2\pi St_{cw}/k_{cw} = 1.732$. Additionally, the spectra also display the second and third harmonics of the dominant peak.

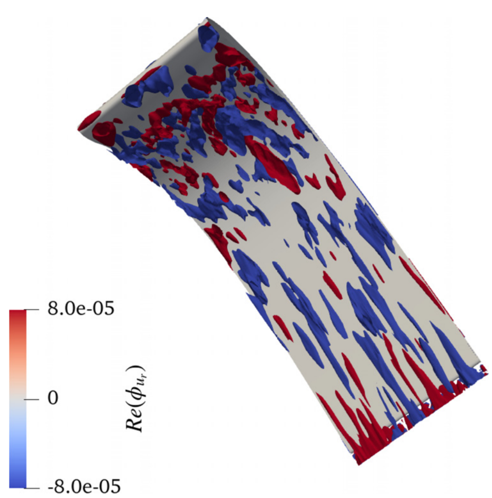

FIG. 7. Streamwise-oriented streaky structures on the blade pressure side, observed in the leading SPOD mode shapes at $St = 1.323$ for the steady inflow case. Flow structures are visualized via isosurfaces colored by the real part of the streamwise velocity component.

B. In the turbine blade domain

In this section, SPOD is applied to flow snapshots obtained exclusively from the turbine blade domain. Although the upstream cylinder is excluded from the volume of interest, its impact is already incorporated in the numerical simulations through communications between the two overlapping meshes, as explained in Sec. III. Consequently, SPOD in this domain captures flow structures associated with the blade boundary layer, passage, and wakes downstream of the blade's trailing edge, impacted by the incoming wakes and FST. To reduce the computational cost of applying SPOD to the full three-dimensional

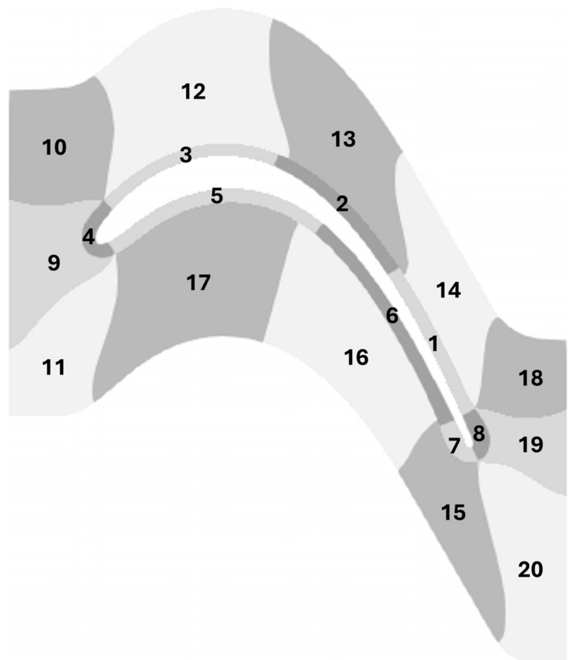

FIG. 8. The turbine blade domain is divided into 20 sub-zones, distributing a similar number of grid points to each zone. The zones are distinguished by randomly assigned colors to clearly differentiate adjacent zones. Zones 1–8 correspond to the blade boundary layer region.

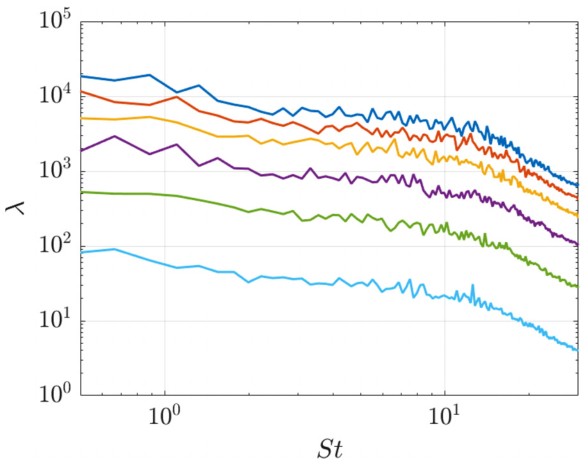

FIG. 9. SPOD energy spectra from flow fluctuations in zone 20 for the steady inflow case. While no tonal peaks are present, spectra around $St = [5, 15]$ exhzibit broadband characteristics.

data with two velocity components, the portion of the domain near the outlet is excluded. To manage memory more efficiently, the Fourier-transformed data are pre-saved, segmented into multiple frequency blocks, and then accessed *one frequency at a time* to perform POD at each specific frequency.

1. Tonal component associated with the cylinder passage

Figure 13 shows the SPOD energy spectra derived within the turbine blade domain. Similar to the results obtained in the cylinder domain (see Fig. 11), a strong peak is registered at the cylinder passage frequency $St = 1.323$. The leading mode at this frequency captures

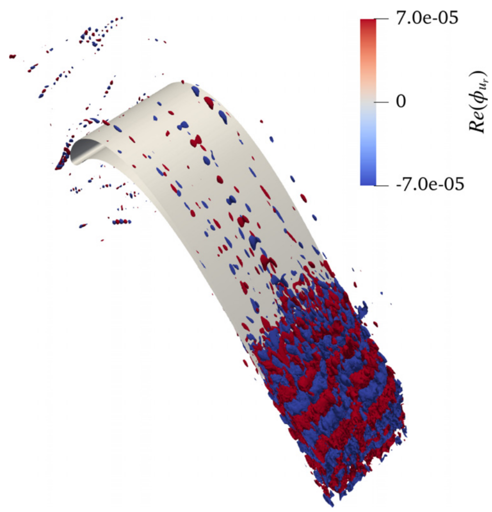

FIG. 10. The leading SPOD modes extracted at $St = 10.60$ for the steady inflow case, visualized via isosurfaces colored by the real part of the streamwise velocity component.

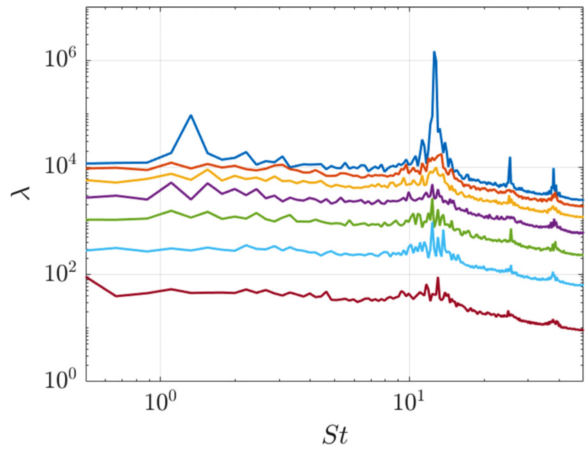

FIG. 11. SPOD energy spectra obtained from flow fluctuations downstream of the moving cylinder, concerning both the axial and the transverse velocity components. Distinct peaks correspond to the cylinder passage frequency at $St = 1.323$, the wakes shedding frequency at $St = 12.57$, and its harmonics.

about 18.43% of the total energy in the system globally, accounting for 93.66% of the energy at this frequency alone. While the cylinder wakes mode at $St_{cw} = 12.57$ dominated the flow dynamics in the previous sub-section, here the cylinder passage moodellens the highest energy, as this mode is underpinned by periodic forcing due to the migration of the energetic wakes into the current reference frame. In contrast, in the cylinder's reference frame, the effects of the periodicity were

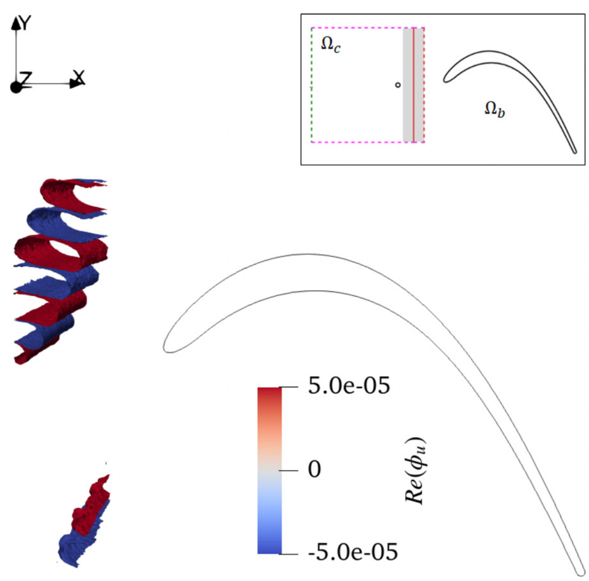

FIG. 12. The leading SPOD mode is visualized using isosurfaces of the real part of the axial velocity component at $St = 12.57$. The LPT blade is included to illustrate the relative position of the cylinder wake structures with respect to the blade. The computational domain used for SPOD analysis is highlighted by the gray-shaded region in the box at the upper right corner. The red solid line within the shaded area denotes the inlet of the turbine domain.

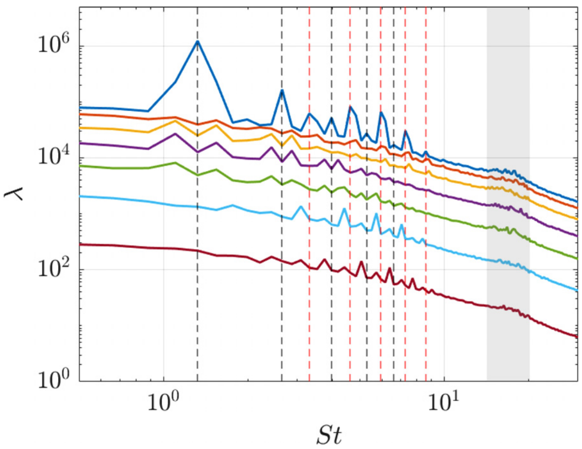

FIG. 13. SPOD energy spectra obtained from the flow fluctuations in the turbine blade domain, concerning both the axial and the transverse velocity fluctuations. Black dashed lines mark the fundamental cylinder passage frequency and its harmonics, while red dashed lines indicate intermediate peaks appearing between the cylinder passage components. A slight bump in the high-frequency range is shaded in gray.

reflected through the stagnation of the cylinder wakes on the blade leading edge, resulting in a smaller energy contribution of this frequency mode. The spectra also display the second through fifth harmonics of the fundamental cylinder passage frequency. Beyond the third harmonic, the contribution of these harmonics to the TKE diminishes, while several intermediate peaks, indicated by red dashed lines, emerge.

Figure 14(a) visualizes the leading SPOD mode at $St = 1.323$ via isosurfaces of the real part of the streamwise velocity component. Large-scale vortical structures align with the direction of the cylinder wakes and migrate toward the blade suction side, ultimately exiting at the trailing edge without further generating new flow structures. These modes bear a close resemblance to those identified from POD performed by Lengani *et al.*[28] and exhibit the bowing and stretching of the incoming wakes in the inter-blade region.[5,25,26,28,29] At this frequency, the wake structures extend across the entire blade span. For higher harmonic modes, the mode shape remains generally similar but appears at smaller scales, as illustrated in Figs. 14(b) and 14(c).

2. Intermediate tones

In the intervals between successive harmonics of the cylinder passage frequency, additional strong peaks emerge at $St = 3.308, 4.631, 5.954$, and 7.278, as indicated by red dashed lines in Fig. 13. These peaks are evenly spaced with an interval of $\Delta St = 1.323$, exactly matching the cylinder passage frequency. Interestingly, these intermediate peaks were not observed in the companion experiment[29] or in similar numerical studies,[34] and their origin remains uncertain. To assess whether they could be numerical errors, we tested the convergence of the SPOD modes computed by varying the number of snapshots per SPOD block, N_{fft}. Regardless of the of the choice of N_{fft}, the intermediate peaks persisted in the spectra

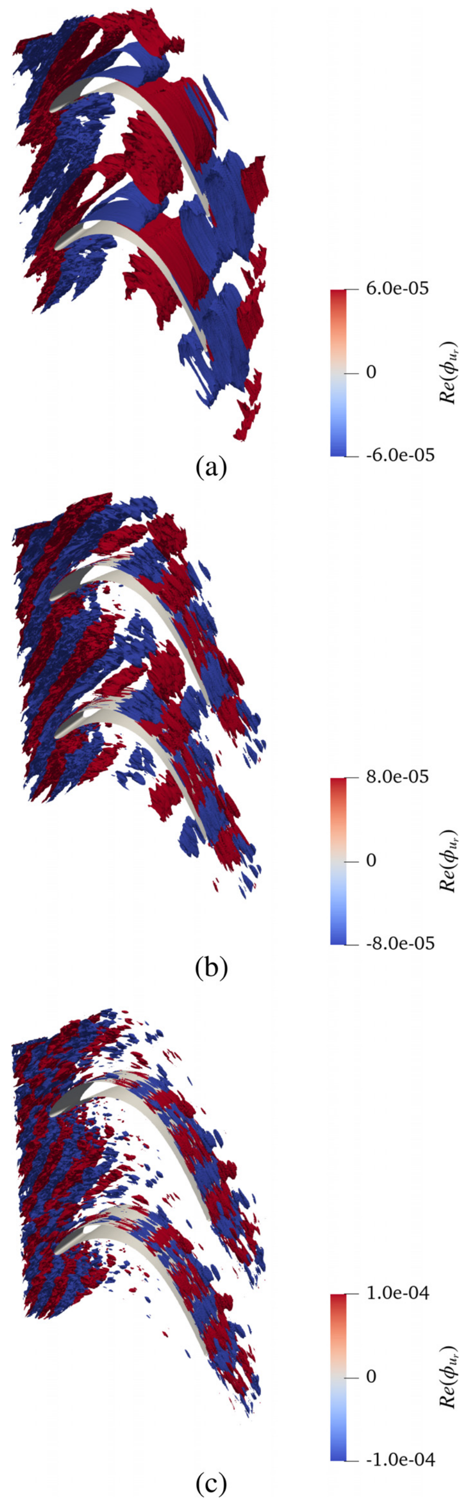

FIG. 14. The leading SPOD modes associated with the cylinder passage at (a) $St = 1.323$, (b) $St = 2.646$, and (c) $St = 3.969$. Mode shapes are visualized via isosurfaces colored by the real part of the streamwise velocity component.

(see Fig. 15), suggesting that convergence issues are not responsible for their appearance.

To investigate the physical origins of each intermediate peak more precisely, we again repeat SPOD on different sections of the turbine blade domain. It is expected that the impact of vortices embedded within the upstream cylinder wakes is most prominent near the leading edge and within the inter-blade region, while the migration of the low momentum area characterizing the incoming wakes affects the entire flow field; wakes and FST potentially influence the blade boundary layers, and wakes are also shed downstream of the trailing edge. Therefore, examining the occurrence of these peaks in specific zones can unveiling their origins.

Figure 16 demonstrates that only the regions around the leading edge exhibit pronounced peaks at these intermediate frequencies, indicating a connection between these components and the incoming cylinder wakes. Notably, their amplitudes are now comparable to that of the cylinder passage peak at $St = 1.323$, reaching the same order of magnitude.

Examples of the leading SPOD modes selected at some of the intermediate frequencies are presented in Fig. 17. In the streamwise component, the modes display strong vortical structures inclined nearly orthogonally to the direction of the cylinder wakes upstream of the blade leading edge. These structures resemble the cylinder wakes, approaching or just impinging the blade leading edge, as depicted in the phase-averaged contours provided in Fig. 7 of De Vincentiis *et al.*[36] Additionally, weak streaky structures emerge in the blade boundary layer on the suction side, just past the leading edge.

Figure 18 provides a closer view of these mode shapes within the blade boundary layers (showing zones 1–8 only). While the incoming wakes have a significant impact at these frequencies, coherent structures also develop on the rear suction side of the blade. Streamwise-oriented low- and high-velocity structures, resembling Klebanoff modes, appear in both velocity component modes. Near to the trailing edge, turbulent

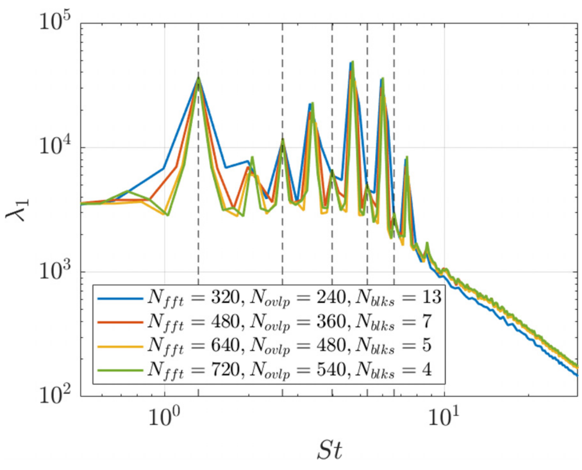

FIG. 15. SPOD energy spectra obtained by applying SPOD to the region upstream of the leading edge (zone 10). The convergence of the leading SPOD mode was examined by varying the number of snapshots per SPOD block (N_{fft}). To facilitate this analysis, only the streamwise velocity perturbations were considered. Black dashed lines indicate the fundamental cylinder passage frequency and its harmonics, serving as a reference for the intermediate tones between them.

spots lacking specific orientation and lambda vortices, typical indicators of turbulent boundary layers, are occasionally observed (as highlighted by black dashed circles in Fig. 18). Here, the shape factor $H_{1,2}$, defined as the ratio of displacement thickness δ^* to momentum thickness θ, has been found to drop toward 1.6, which is slightly higher than a value typical of turbulent flows (not shown for brevity). Furthermore, similar streaky structures also appear on the blade pressure side, as illustrated in Fig. 19. Consequently, these intermediate frequency modes are thought to capture the interaction of the upstream cylinder wakes and FST with the blade boundary layers, forming streaks whose breakdown promotes the transition to turbulence.

While the mode shapes closely resemble those of the cylinder wakes, these peaks appear at frequencies that deviate significantly from the cylinder wake shedding frequency of $St_{cw} = 12.57$, identified by SPOD in the cylinder domain in the previous section. This deviation complicates the interpretation of the physical significance of these modes. However, analyzing the phase velocity of the upstream cylinder wakes provides insights into their origin, revealing that these modes are indeed associated with the propagation of the wakes, which become Doppler-shifted due to the passage of the cylinder.

In Sec. VI A, it was found that the cylinder wakes propagate with a phase speed of $u_{p,cw} = 1.732$ in the cylinder's reference frame, considering that they are aligned with the relative velocity u_{rel}. As depicted in Fig. 20(a), the direction of the propagation angle β is estimated as

$$\beta = \tan^{-1}\left(\frac{u_{in}\sin\alpha + u_c}{u_{in}\cos\alpha}\right) = 66.81^\circ, \tag{7}$$

which closely matches the measured value from the corresponding leading SPOD mode. On the other hand, when viewed in the turbine frame (see Fig. 20), the LPT blade perceives these incoming wakes at a modified angle β' given by

$$\beta' = \tan^{-1}\left(\frac{u_{p,cw}\sin\beta - u_c}{u_{p,cw}\cos\beta}\right) = 33.24^\circ, \tag{8}$$

again assuming that the wakes align in the mean flow direction. The modified phase speed is similarly computed as

$$u'_{p,cw} = \sqrt{\left(u_{p,cw}\sin\beta - u_c\right)^2 + \left(u_{p,cw}\cos\beta\right)^2} = 0.8155. \tag{9}$$

For a source (the cylinder) translating vertically at a speed of $u_s = u_c = 1.145$ and incident to a stationary observer (the blade) at an angle of $\beta' = 33.24^\circ$, the Doppler-shifted frequency can be calculated as

$$f = \left(\frac{u \pm u_r}{u \pm u_s}\right) f_0 = \left(\frac{u'_{p,cw}}{u'_{p,cw} + u_c \sin\beta'}\right) f_0 = 7.103, \tag{10}$$

where u is the phase speed of the cylinder wakes $u'_{p,cw}$ computed above, u_r is the observer's velocity, u_s represents the source velocity (the moving cylinder), and f_0 corresponds to the cylinder wakes shedding frequency. Here, f represents a dimensionless frequency, equivalent to the Strouhal number St. Note that all velocities are estimated in the reference frame of turbine, assuming that the wakes propagate in the direction of the mean flow. Furthermore, the case where the cylinder wakes approach toward the turbine blade (i.e., a positive sign in the

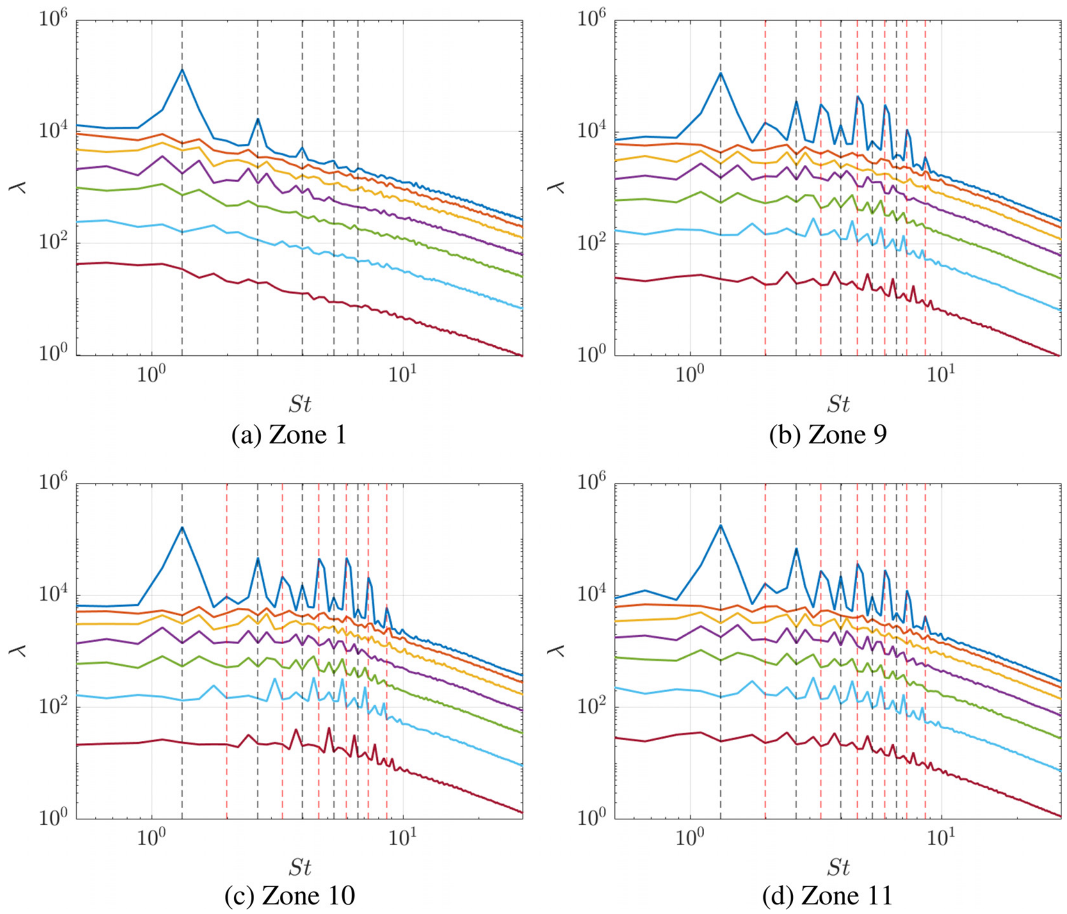

FIG. 16. SPOD energy spectra obtained by applying SPOD to each sub-domain. Black dashed lines mark the fundamental cylinder passage frequency and its harmonics, while red dashed lines indicate intermediate peaks appearing between the cylinder passage components. Note that the intermediate peaks emerge only in the spectra of the zones located upstream of the leading edge (b, c, d).

denominator) is ignored, as it would result in a shifted frequency outside the relevant frequency for the present analysis.

Finally, triadic interactions between the modes associated with the cylinder passage at $St = 1.323$ and the Doppler-shifted cylinder wakes at $St = 7.103$ may further yield a cascade of energetic modes distributed uniformly with $\Delta St = 1.323$, appearing at $St = [5.783, 4.460, 3.137]$. Considering uncertainties that may arise from limited frequency resolution and wavenumber resolution, with the latter resulting from the restricted spatial extent in the cylinder domain when estimating the phase speed of the cylinder wakes, these values are considered quite close to the peaks registered at $St = [5.954, 4.631, 3.308]$ in the SPOD energy spectra shown in Fig.13.

The bispectrum map further confirms strong triadic interactions between the modes associated with these frequencies and $St = 1.323$, reinforcing the idea that the vortical structures orthogonal to the main cylinder wake direction are directly tied to the Doppler-shifted wakes by the cylinder's translation. Theoretically, the bispectrum detects triadic nonlinear interactions, a fundamental mechanism for energy transfer process in fluid flows. In this study, we consider the mode bispectrum, a variant of the classical bispectrum, computed through bispectral mode decomposition (BMD).[50] Unlike the classical bispectrum, the mode bispectrum derived via BMD allows consideration of causal relationships between frequency components involved in triadic interactions. BMD maximizes the pointwise bispectral density of a fluctuating flow field $\mathbf{q}$ defined over the spatial domain Ω, as expressed by

$$b(f_k, f_l) = E\left[\int_\Omega \hat{\mathbf{q}}_k^* \circ \hat{\mathbf{q}}_l^* \circ \hat{\mathbf{q}}_{k+l} d\mathbf{x}\right] = E[\hat{\mathbf{q}}_{k\circ l}^H \mathbf{W} \hat{\mathbf{q}}_{k+l}], \qquad (11)$$

where $\hat{\mathbf{q}}$ is the Fourier transform of $\mathbf{q}$, $(\cdot)^*$ denote the scalar complex conjugate, the operator $\circ$ represents the Hadamard (element-wise) product, and H indicates the complex transpose. The matrix W is a diagonal matrix that incorporates spatial quadrature weights. Additionally, f is a frequency with subscripts k and l serving as indices for frequency doublets. Using Welch's method, the Fourier transforms of flow snapshots are assembled into data matrices $\hat{\mathbf{Q}}_{k\circ l}$ and $\hat{\mathbf{Q}}_{k+l}$ defined as

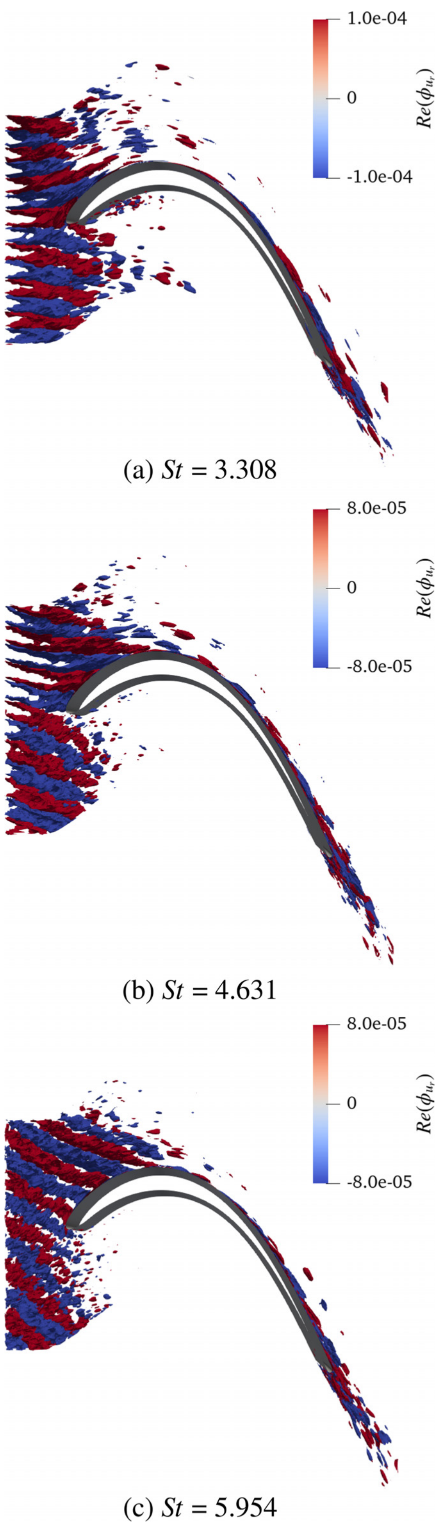

FIG. 17. The leading SPOD mode extracted at three selected intermediate peak frequencies. Mode shapes are visualized via isosurfaces colored by the real part of the streamwise velocity components.

$$\hat{\mathbf{Q}}_{k\circ l} = \begin{bmatrix} \hat{\mathbf{q}}_{k\circ l}^{[1]} & \hat{\mathbf{q}}_{k\circ l}^{[2]} & \dots & \hat{\mathbf{q}}_{k\circ l}^{[N_{blk}]} \end{bmatrix} \tag{12}$$

and

$$\hat{\mathbf{Q}}_{k+l} = \begin{bmatrix} \hat{\mathbf{q}}_{k+l}^{[1]} & \hat{\mathbf{q}}_{k+l}^{[2]} & \dots & \hat{\mathbf{q}}_{k+l}^{[N_{blk}]} \end{bmatrix}, \tag{13}$$

where N_{blk} is the total number of snapshots blocks. Subsequently, the auto-bispectral density matrix $\mathbf{B}$ is introduced as

$$\mathbf{B} = \frac{1}{N_{blk}} \hat{\mathbf{Q}}_{k\circ l}^{H} \mathbf{W} \hat{\mathbf{Q}}_{k+l}. \tag{14}$$

Note that the matrix $\mathbf{B}$ is non-Hermitian. The complex mode bispectrum is then obtained by solving the following maximization problem:

$$\lambda_1(f_k, f_l) = \max \left| \frac{\mathbf{a}_1^H \mathbf{B} \mathbf{a}_1}{\mathbf{a}_1^H \mathbf{a}_1} \right|, \tag{15}$$

where $\mathbf{a}_1$ represents the optimal expansion coefficient. Further details including the computation of bispectral modes (not shown here) can be found in Schmidt.[50]

Figure 21 shows the magnitude of the mode bispectrum computed using the LPT DNS data. Here, single-component (streamwise) velocity data from the region upstream of the leading edge (zone 10 in Fig. 8) is used to facilitate testing. While the original map spans wider cross-frequency ranges, only a portion is shown for brevity, with black circles highlighting the six strongest triadic interactions. The abscissa and ordinate of the figure represent frequency doublets $\{St_k, St_l\}$ associated with each triadic interaction. The first quadrant accordingly describes sum-interactions, while the fourth quadrant quantifies difference-interactions. Distinct diagonal lines with a slope of -1 represent each constant frequency component generated by such triadic interactions.

From Fig. 21, one can first observe intense difference-interactions leading to flow structures related to the cylinder passage frequency (e.g., $\{St_k, -St_l, St_k - St_l\} = \{5.954, -4.631, 1.323\}$ and $\{4.631, -3.308, 1.323\}$) along the black dashed diagonal line. Sum- and difference-interactions between the modes corresponding to the Doppler-shifted cylinder wake components (St_k=[5.954,4.631, 3.308]) and the cylinder passage frequency (St_l=1.323), which generate a cascade of new Doppler-shifted cylinder wake modes ($St_k \pm St_l$), are also noticeable along the two high-amplitude horizontal lines. Interactions between the mode captured at St=7.103 (the fundamental Doppler-shifted cylinder wakes frequency) and the cylinder passage mode are also detected, though they appear less pronounced than the cascade of the above-mentioned triadic interactions. While a conclusive explanation is not available, it may be zone-dependent.

Unlike in Fiore *et al.*,[34] the shifted frequencies appear at much lower values, separated from the broadband spectrum associated with the trailing edge von Kármán vortex streets. In their study, the upstream structures that were nearly orthogonal to the cylinder wake direction were found within the broadband spectrum modes linked to the blade trailing edge wakes, but they did not establish an explicit connection between the cylinder wake shedding frequency and these modes. The differences between our results and those of Fiore *et al.*[34] may stem from variations in flow configuration and simulation resolution. In our case, the upstream cylinder is positioned much closer to the blade, which may allow the Doppler-shifted cylinder wake modes to carry relatively higher energy content.

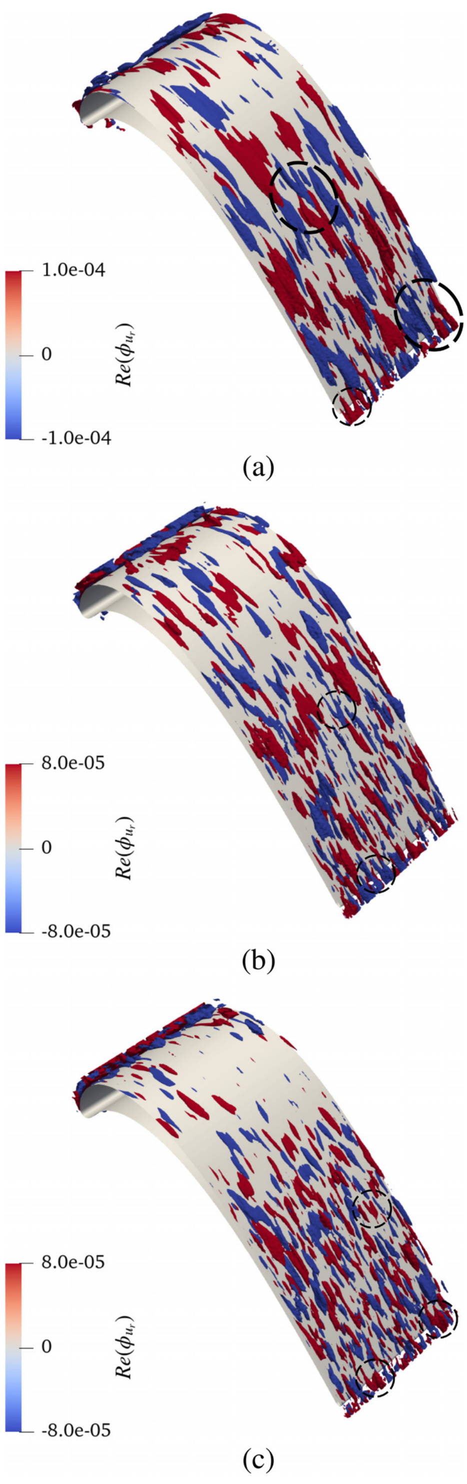

FIG. 18. The leading SPOD mode extracted at three selected intermediate peak frequencies, zoomed in close to the blade boundary layer region: (a) $St = 3.308$, (b) $St = 4.631$, and (c) $St = 5.954$. Mode shapes are visualized via isosurfaces colored by the real part of the streamwise velocity component.

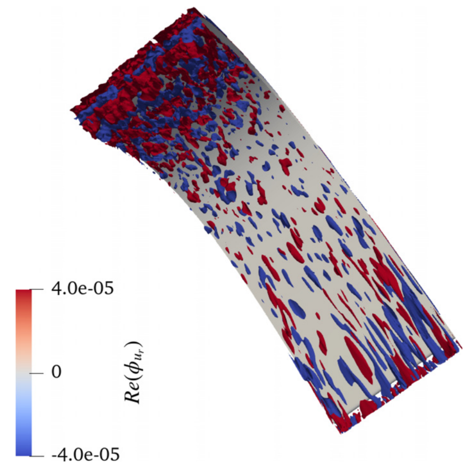

FIG. 19. The leading SPOD mode shape around the rear pressure side of the blade at $St = 3.308$, visualized with isosurfaces colored by the real part of the streamwise velocity component.

3. High-frequency broadbanded part

The amplitudes of the SPOD eigenvalues continue to decrease at high frequencies, with a slight bump observed between $St = [14, 20]$. This broadband portion corresponds to the vortex shedding at the blade trailing edge, similar to what is seen in the steady inflow case. By applying SPOD on a zonal basis, this feature is detectable only in the zones adjacent to the trailing edge (zones 7, 8, 15, 19, and 20 in Fig. 8). Within this frequency range, the energy spectra exhibit slight elevations, but the modes remain significantly weaker than those associated with the cylinder wakes.

Figure 22 visualizes some of the leading SPOD modes extracted within this frequency range. The streamwise velocity component reveals fine-scale flow structures in the blade upstream and some trailing edge vortex rolls. Across the broadband frequency range, the

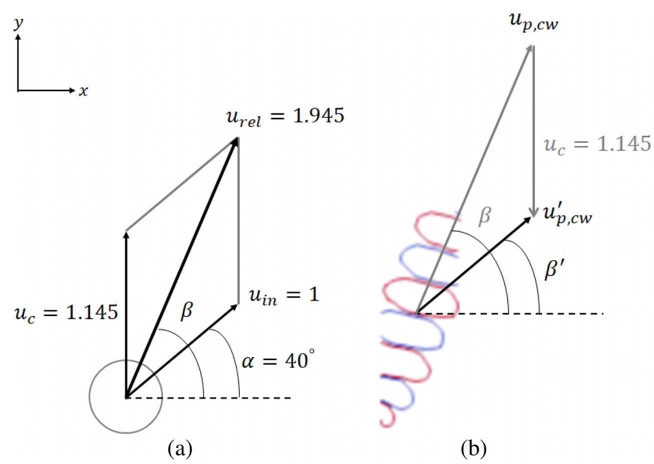

FIG. 20. Schematics illustrating the estimation of (a) the relative velocity as observed in the cylinder domain and (b) the phase velocity of the upstream cylinder wakes in the turbine reference frame. The figures are not drawn to scale.

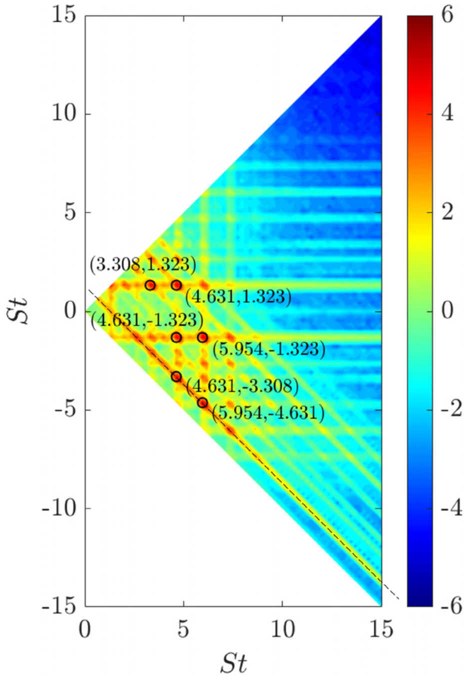

FIG. 21. (Magnitude) mode bispectrum $\log(|\lambda_1|)$ for the incoming cylinder wakes. The analysis is restricted to zone 10, the region located upstream of the blade leading edge. The mode bispectrum is computed with $N_{blk} = 480$ using data from the streamwise velocity component. Black circles highlight the six strongest triadic interactions. The black dashed diagonal line represents the cylinder passage frequency $St = 1.323$.

upstream structures related to the cylinder wakes are generally stronger than the trailing edge shedding vortices. However, at higher frequencies, the trailing edge rolls become more pronounced with stronger amplitudes. The spanwise length scale of the vortices is less than the blade half-span. Influenced by both elevated freestream turbulence and incoming wakes, the vortex train is released exclusively downstream of the blade, showing no evidence of laminar separation before exiting the trailing edge, akin to a bypass-type transition.

For the trailing edge thickness of $t = 0.02g = 0.0173c_x$ and the downstream velocity $u_{ext} = 1.594$, the broadband frequency range is converted as

$$St_t = \frac{ft}{u_{ext}} = \frac{fc_x}{u_{in}}\frac{t}{c_x}\frac{u_{in}}{u_{ext}} = St\frac{t}{c_x}\frac{u_{in}}{u_{ext}} \approx [0.152, 0.217]. \qquad (16)$$

This result is situated near the lower end of the range $0.2 < St_t < 0.4$, which typically represents cases where the blade boundary layers are turbulent on both the suction and pressure sides, as reported in the literature.[51,52] This aligns well with the turbulent spots and hairpin-like structures observed on the suction side in experiments, as well as those documented in De Vincentiis *et al.*[36] Note that our blade has a relatively sharp edge, which may yield the lower St_t value.

VII. CONCLUSIONS

In this work, SPOD is applied to DNS data of an LPT cascade subjected to high FST intensities. To evaluate the impact of periodic incoming wakes on boundary layer transition, DNS datasets for both case—with and without wakes—are utilized. The upstream wakes are modeled by a moving cylinder located upstream of the blade leading edge, as implemented in the companion experiment and numerous other studies. While periodic wakes are commonly imposed as instantaneous inflow conditions in previous DNS studies, the dataset here incorporates a moving cylinder within the computation, simultaneously interacting with the turbine domain simulations through a sliding grid. High-intensity, isotropic FST is achieved by specifying an integral length scale close to the experimental value and scaling wavenumber components to follow the von Kármán energy spectrum. SPOD is then applied to flow snapshots that construct the covariance matrix for both the streamwise and wall-normal velocity components, excluding the spanwise component, which carries significantly less energy than the former two. The TKE across the turbine domain is chosen as the norm to optimize the resulting SPOD modes, as the local Mach number within the LPT system remains below 0.1.

In the absence of upstream wakes, the resulting SPOD spectra display nearly monotonically decreasing eigenvalues with increasing frequency. The spectra broaden slightly over a range of $St = [5, 15]$,

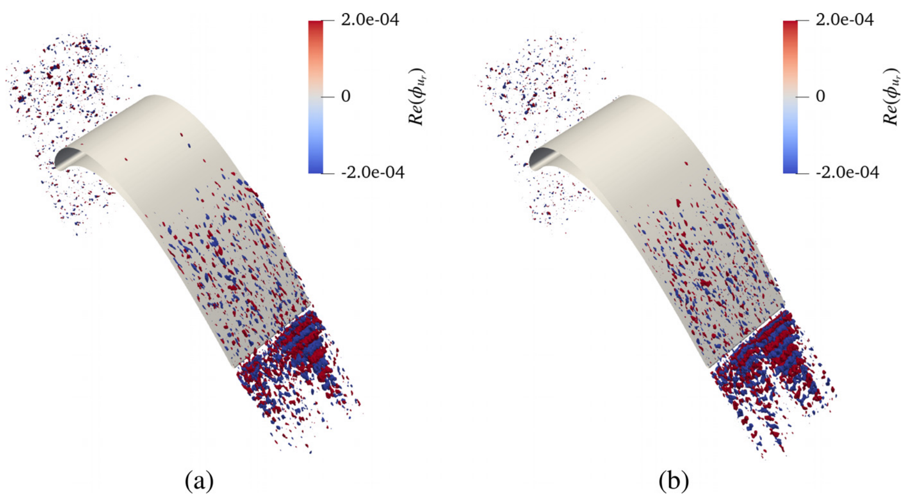

FIG. 22. The leading SPOD shapes visualized by isosurfaces colored by the real part of the streamwise velocity component: (a) $St = 16.54$ and (b) $St = 17.86$.

corresponding to the Kármán vortex streets formed downstream of the trailing edge. SPOD modes are visualized with isosurfaces colored by the real part of either the streamwise or the wall-normal velocity components. Across the resolvable frequency range, the mode shapes reveal fully attached boundary layers along the blade, indicating that elevated FST levels effectively suppress boundary layer separation. Low- and high-velocity streaky structures are observed at low to mid frequencies, attributed to the influence of the high FST intensities.

Under the influence of upstream wakes, the SPOD energy spectra show several energetic modes. The most prominent tone at $St = 1.323$ corresponds to the passage of the upstream cylinder and is associated with the development of turbulent spots and lambda vortices on the rear suction side of the blade, typical indicatives of turbulent boundary layers. SPOD modes at these low frequencies illustrate large-scale vortical structures that stretch and migrate toward the inter-blade region and the blade boundary layer. In addition, a series of intermediate tones appear between the fundamental passage frequency and its harmonics, corresponding to Doppler-shifted wakes emphasized due to the proximity between the cylinder and the blade. These modes are a result of triadic interactions between the wakes and the cylinder's movement, as further confirmed by plotting the mode bispectrum map computed using the open-source BMD code. The corresponding modes shape into low- and high-velocity streaky structures in the streamwise direction on the blade's rear suction side. Breakdown of the streaks leads to the transition in this case and is described as the trailing edge vortex streets at high frequencies, similarly in the steady inflow case. The corresponding mode shapes form low- and high-velocity streaky structures oriented in the streamwise direction on the rear suction side of the blade. In this case, the breakdown of these streaks initiates transition, generating trailing edge vortex streets at higher frequencies, similarly observed in the steady inflow scenario.

While POD turn out to be an effective tool to identify and quantify dominant flow structures related to the transition process of the LPT blades, comparison of the SPOD results for the inflow conditions with or without upstream wakes clearly distinguish their spectral characteristics. For both inflow conditions, the understanding of the full domain SPOD modes is enhanced by applying SPOD to 20 sub-zones, each designed to capture the unique physical mechanisms in different regions of the LPT domain. High-frequency broadband part appears in the zones close to the blade trailing edge only, while the low-frequency spectral peaks, particularly the intermediate tones, are apparent in the zones near the blade leading edge.

While POD has proven effective for identifying and quantifying dominant flow structures linked to the transition process in LPT blades, comparing SPOD results for inflow conditions with and without upstream wakes highlights clear spectral differences between the two. For both inflow cases, understanding of the full-domain SPOD modes is enhanced by performing SPOD on 20 sub-zones, each decomposed to capture unique physical mechanisms within different regions of the LPT domain. High-frequency broadband components appear only in the zones near the blade trailing edge, whereas low-frequency intermediate spectral peaks are prominent in zones closer to the blade leading edge. Tones related to the cylinder passage influence all 20 zones.

The interpretation of the intermediate peaks emerging under unsteady inflow conditions is further clarified by the bispectrum map. In fact, BMD can capture spatially coherent structures linked to these interactions, generating an interaction map that pinpoints areas where each triadic event is most significant.[50] While this approach may offer valuable insights into energy transfer within the LPT system, it extends beyond the scope of this work.

ACKNOWLEDGMENTS

This study is part of an ongoing collaboration between research teams from KTH Royal Institute of Technology and the University of Genova. The work initiated during J.J.'s visit to the University of Genova, supported by funding from the HPC-Europa3 program. We acknowledge Kristina Đurović and Luca De Vincentiis for kindly providing the DNS data used in this study. The computations and data handling were enabled by resources provided by the National Academic Infrastructure for Supercomputing in Sweden (NAISS), partially funded by the Swedish Research Council (Grant Agreement No. 2022-06725).

AUTHOR DECLARATIONS

Conflict of Interest

The authors have no conflicts to disclose.

Author Contributions

Jinah Jeun: Conceptualization (equal); Data curation (lead); Formal analysis (lead); Investigation (lead); Methodology (lead); Software (lead); Visualization (lead); Writing – original draft (lead). **Davide Lengani:** Conceptualization (equal); Investigation (supporting); Writing – review & editing (equal). **Jan Oscar Pralits:** Conceptualization (equal); Investigation (supporting); Writing – review & editing (equal). **Daniele Simoni:** Conceptualization (equal); Investigation (supporting); Writing – review & editing (equal). **Ardeshir Hanifi:** Conceptualization (equal); Formal analysis (supporting); Investigation (supporting); Project administration (supporting); Resources (supporting); Supervision (equal); Writing – review & editing (equal). **Dan Henningson:** Conceptualization (equal); Funding acquisition (lead); Investigation (supporting); Project administration (lead); Resources (lead); Supervision (equal); Writing – review & editing (equal).

DATA AVAILABILITY

The data that support the findings of this study are available from the corresponding author upon reasonable request.

REFERENCES

[1] H. P. Hodson and R. J. Howell, "The role of transition in high-lift low-pressure turbines for aeroengines," Prog. Aerosp. Sci. **41**, 419–454 (2005).
[2] R. D. Sandberg and V. Michelassi, "Fluid dynamics of axial turbomachinery: Blade- and stage-level simulations and models," Annu. Rev. Fluid Mech. **54**, 255–285 (2022).
[3] J. G. Wissink, "DNS of separating, low Reynolds number flow in a turbine cascade with incoming wakes," Int. J. Heat Fluid Flow **24**, 626–635 (2003).
[4] M. Lang, U. Rist, and S. Wagner, "Investigations on controlled transition development in a laminar separation bubble by means of LDA and PIV," Exp. Fluids **36**, 43–52 (2004).
[5] R. D. Stieger and H. P. Hodson, "The unsteady development of a turbulent wake through a downstream low-pressure turbine blade passage," J. Turbomach. **127**, 388–394 (2005).

[6]S. Burgmann and W. Schröder, "Investigation of the vortex induced unsteadiness of a separation bubble via time-resolved and scanning PIV measurements," Exp. Fluids **45**, 675–691 (2008).
[7]D. Simoni, M. Ubaldi, P. Zunino, D. Lengani, and F. Bertini, "An experimental investigation of the separated-flow transition under high-lift turbine blade pressure gradients," Flow. Turbul. Combust. **88**, 45–62 (2012).
[8]D. Lengani and D. Simoni, "Recognition of coherent structures in the boundary layer of a low-pressure-turbine blade for different free-stream turbulence intensity levels," Int. J. Heat Fluid Flow **54**, 1–13 (2015).
[9]R. G. Jacobs and P. A. Durbin, "Shear sheltering and the continuous spectrum of the Orr–Sommerfeld equation," Phys. Fluids **10**, 2006–2011 (1998).
[10]P. S. Klebanoff, "Effect of free-stream turbulence on a laminar boundary layer," Bull. Am. Phys. Soc. **16**, 1323 (1971).
[11]J. Kendall, "Experimental study of disturbances produced in a pre-transitional laminar boundary layer by weak freestream turbulence," AIAA Paper No. 85–1695 (1985).
[12]K. J. A. Westin, A. V. Boiko, B. G. B. Klingmann, V. V. Kozlov, and P. H. Alfredsson, "Experiments in a boundary layer subjected to free stream turbulence. Part 1. Boundary layer structure and receptivity," J. Fluid Mech. **281**, 193–218 (1994).
[13]M. Matsubara and P. H. Alfredsson, "Disturbance growth in boundary layers subjected to free-stream turbulence," J. Fluid Mech. **430**, 149–168 (2001).
[14]P. Andersson, M. Berggren, and D. S. Henningson, "Optimal disturbances and bypass transition in boundary layers," Phys. Fluids **11**, 134–150 (1999).
[15]P. Luchini, "Reynolds-number-independent instability of the boundary layer over a flat surface: Optimal perturbations," J. Fluid Mech. **404**, 289–309 (2000).
[16]P. Schlatter, L. Brandt, H. C. De Lange, and D. S. Henningson, "On streak breakdown in bypass transition," Phys. Fluids **20**, 101505 (2008).
[17]M. Dellacasagrande, D. Lengani, D. Simoni, J. O. Pralits, K. Durovich, A. Hanifi, and D. Henningson, "Statistical characterization of free-stream turbulence induced transition under variable Reynolds number, free-stream turbulence, and pressure gradient," Phys. Fluids **33**, 094115 (2021).
[18]K. Ðurović, A. Hanifi, P. Schlatter, K. Sasaki, and D. S. Henningson, "Direct numerical simulation of transition under free-stream turbulence and the influence of large integral length scales," Phys. Fluids **36**, 074105 (2024).
[19]M. T. Landahl, "A note on an algebraic instability of inviscid parallel shear flows," J. Fluid Mech. **98**, 243–251 (1980).
[20]R. G. Jacobs and P. A. Durbin, "Simulations of bypass transition," J. Fluid Mech. **428**, 185–212 (2001).
[21]B. R. McAuliffe and M. I. Yaras, "Transition mechanisms in separation bubbles under low- and elevated-freestream turbulence," J. Turbomach. **132**, 011004 (2010).
[22]T. A. Zaki, "From streaks to spots and on to turbulence: Exploring the dynamics of boundary layer transition," Flow Turbul. Combust. **91**, 451–473 (2013).
[23]L. Brandt, "The lift-up effect: The linear mechanism behind transition and turbulence in shear flows," Eur. J. Mech. B/Fluids **47**, 80–96 (2014).
[24]A. Dotto, M. Luzzi, J. Verdoya, D. Simoni, A. Hanifi, and J. O. Pralits, "Stability of low-pressure turbine boundary layers under variable Reynolds number and pressure gradient," Phys. Fluids **36**, 034116 (2024).
[25]X. Wu and P. A. Durbin, "Evidence of longitudinal vortices evolved from distorted wakes in a turbine passage," J. Fluid Mech. **446**, 199–228 (2001).
[26]V. Michelassi, J. Wissink, and W. Rodi, "Analysis of DNS and LES of flow in a low pressure turbine cascade with incoming wakes and comparison with experiments," Flow Turbul. Combust. **69**, 295–329 (2002).
[27]S. Sarkar, "Identification of flow structures on a LP turbine blade due to periodic passing wakes," J. Fluids Eng. **130**, 061103 (2008).
[28]D. Lengani, D. Simoni, R. Pichler, R. D. Sandberg, V. Michelassi, and F. Bertini, "Identification and quantification of losses in a LPT cascade by POD applied to LES data," Int. J. Heat Fluid Flow **70**, 28–40 (2018).
[29]D. Lengani, D. Simoni, M. Ubaldi, P. Zunino, and F. Bertini, "Coherent structures formation during wake-boundary layer interaction on a LP turbine blade," Flow Turbul. Combust. **98**, 57–81 (2017).
[30]Y. Zhao and R. D. Sandberg, "High-fidelity simulations of a high-pressure turbine stage: Effects of Reynolds number and inlet turbulence," in *ASME Turbo Expo: Turbomachinery Technical Conference and Exposition* (ASME, 2021).
[31]J. Leggett, S. Priebe, A. Shabbir, V. Michelassi, R. Sandberg, and E. Richardson, "Loss prediction in an axial compressor cascade at off-design incidences with free stream disturbances using large eddy simulation," J. Turbomach. **140**, 071005 (2018).
[32]J. L. Lumley, "The structure of inhomogeneous turbulent flows," in *Atmospheric Turbulence and Radio Wave Propagation*, edited by A. M. Yaglom and V. I. Tartarsky (Nauka, 1967), pp. 166–178.
[33]D. Lengani, D. Simoni, M. Ubaldi, P. Zunino, and F. Bertini, "Recognition of structures leading to transition in a low-pressure turbine cascade: Effect of reduced frequency," J. Turbomach. **142**, 061007 (2020).
[34]M. Fiore, R. Gojon, G. Sáez-Mischlich, and J. Gressier, "LES of the T106 low-pressure turbine: Spectral proper orthogonal decomposition of the flow based on a fluctuating energy norm," Comput. Fluids **252**, 105761 (2023).
[35]D. Biassoni, M. Russo, and D. Lengani, "A high-performance code for the use of spectral pod on the analysis of turbomachinery high fidelity simulations," Proceedings of Global Power and Propulsion Society (2024).
[36]L. De Vincentiis, K. Ðurović, D. Lengani, D. Simoni, J. Pralits, D. S. Henningson, and A. Hanifi, "Effects of upstream wakes on the boundary layer over a low-pressure turbine blade," J. Turbomach. **145**, 051011 (2023).
[37]K. Ðurović, L. De Vincentiis, D. Simoni, D. Lengani, J. Pralits, D. S. Henningson, and A. Hanifi, "Free-stream turbulence-induced boundary-layer transition in low-pressure turbines," J. Turbomach. **143**, 081015 (2021).
[38]X. Wu, R. G. Jacobs, J. C. R. Hunt, and P. A. Durbin, "Simulation of boundary layer transition induced by periodically passing wakes," J. Fluid Mech. **398**, 109–153 (1999).
[39]G. Kalitzin, X. Wu, and P. A. Durbin, "DNS of fully turbulent flow in a LPT passage," Int. J. Heat Fluid Flow **24**, 636–644 (2003).
[40]P. F. Fischer, J. W. Lottes, and S. G. Kerkemeier, see http://nek5000.mcs.anl.gov for "Nek5000" (2008).
[41]Y. Maday, C. Mavriplis, and A. Patera, "Nonconforming mortar element methods: Application to spectral discretizations," Report No. NACA-CR-181729, 1988.
[42]P. Schlatter, "Direct numerical simulation of laminar-turbulent transition in boundary layer subject to free-stream turbulence," Diploma thesis (KTH Royal Institute of Technology, 2001).
[43]P. Schlatter, R. Örlü, Q. Li, G. Brethouwer, J. Fransson, A. V. Johansson, P. H. Alfredsson, and D. S. Henningson, "Turbulent boundary layers up to $Re_\theta = 2500$ studied through simulation and experiment," Phys. Fluids **21**, 051702 (2009).
[44]A. Towne, O. T. Schmidt, and T. Colonius, "Spectral proper orthogonal decomposition and its relationship to dynamic mode decomposition and resolvent analysis," J. Fluid Mech. **847**, 821–867 (2018).
[45]P. Welch, "The use of fast Fourier transform for the estimation of power spectra: A method based on time averaging over short, modified periodograms," IEEE Trans. Audio Electroacoust. **15**, 70–73 (1967).
[46]L. Sirovich, "Turbulence and the dynamics of coherent structures. I. coherent structures," Quart. Appl. Math. **45**, 561–571 (1987).
[47]J. H. Lienhard, *Synopsis of Lift, Drag, and Vortex Frequency Data for Rigid Circular Cylinders* (Technical Extension Service, Washington State University, Pullman, WA, 1966), Vol. 300.
[48]S. Chu, C. Xia, H. Wang, Y. Fan, and Z. Yang, "Three-dimensional spectral proper orthogonal decomposition analyses of the turbulent flow around a seal-vibrissa-shaped cylinder," Phys. Fluids **33**, 025106 (2021).
[49]Y. Schubert, M. Sieber, K. Oberleithner, and R. Martinuzzi, "Towards robust data-driven reduced-order modelling for turbulent flows: Application to vortex-induced vibrations," Theor. Comput. Fluid Dyn. **36**, 517–543 (2022).
[50]O. T. Schmidt, "Bispectral mode decomposition of nonlinear flows," Nonlinear Dyn. **102**, 2479–2501 (2020).
[51]C. H. Sieverding and H. Heinemann, "The influence of boundary layer state on vortex shedding from flat plates and turbine cascades," J. Turbomach. **112**, 181–187 (1990).
[52]G. Cicatelli and C. H. Sieverding, "A review of the research on unsteady turbine blade wake characteristics," in AGARD PEP 85th Symposium on Loss Mechanisms and Unsteady Flows in Turbomachinery (1995).